Elastic full-waveform inversion: density effects, cycle-skipping, and inter-parameter mapping

Wenyong Pan, Kris Innanen

ABSTRACT

In this research, we studied the problems when recovering elastic parameters (P-wave velocity, S-wave velocity and density) including cycle-skipping problem, density effect, and inter-parameter crosstalk issue. We find that elastic wave equation trave time method with a cross-correlation misfit function can be employed to build long wavenumber components for P-wave velocity and S-wave velocity, which helps to overcome the cycle-skipping problem in elastic FWI. Then elastic wave equation waveform inversion can be used to provide high resolution estimates of the model parameters. Density is quite difficult to be recovered, which may be caused by its insensitivity to travel time or the inter-parameter trade-off. We also propose to quantify the parameter trade-off by probing the multi-parameter Hessian. The multi-parameter point spread functions, which is proportional to one column of the multi-parameter Hessian, measure the parameter trade-off between different physical parameters more completely compared to traditional studies based on scattering patterns. The studies are verified using numerical examples with reflection survey and transmission survey.

INTRODUCTION

Full-waveform inversion techniques are considered to be promising for providing high-resolution estimates of subsurface properties (Lailly, 1983; Tarantola, 1984; Pratt et al., 1998; Virieux and Operto, 2009). However, because of the lack of low frequencies and inaccurate initial model, even just P-wave velocity is quite difficult to be recovered resulting from the high-nonlinearity of the inverse problem. Researchers devote significant efforts to overcoming the cycle-skipping problem (Ma and Hale, 2012; Warner and Guasch, 2014; Wu et al., 2014; Li and Demanet, 2016; Zhu and Fomel, 2016).

Incorporating elasticity into full-waveform inversion is becoming very necessary, because subsurface media is more appropriate to be described by elasticity and the elastic properties are very important for reservoir characterization. However, recovering multiple elastic parameters is much more challenging (Yanhua and Simons, 2014; Yanhua et al., 2015). The cycle-skipping problem becomes more serious. In this research, we studied the strategies for overcoming the cycle-skipping problems in elastic FWI. The elastic wave equation travel time inversion methods based on a cross-correlation misfit function are carried out first to retrieve the long wavenumber components of the model parameters. The elastic wave equation waveform inversion are then used to provide high-resolution estimates of the elastic properties. This inversion strategy is named as joint elastic wave equation travel time and waveform inversion.

Furthermore, the inter-parameter mapping between different physical parameters result in parameter crosstalk artifacts, which increases the non-linearity of inverse problem significantly. The parameter resolution issues for different parameter classes for multi-parameter

elastic and anisotropic FWI have been studies by many researchers. These studies are carried out based on the scattering patterns, which represent the analytic solutions of the Fréchet derivative wavefields due to different physical parameters. It says that if the scattering patterns due to different physical parameters overlap at certain range of scattering angle, the parameter crosstalk appear within this range of scattering angle. However, we find that these studies based on scattering patterns may not be able to evaluate the parameter resolution due to the inherent defects of the scattering patterns.

In this research, we reveal that the off-diagonal blocks of the multi-parameter Hessian provides the parameter trade-off measurements more completely and directly. With multi-parameter Hessian, we are capable to quantify the parameter resolution by considering geometrical spreading, complex model, finite-frequency effects and etc. However, for large-scale inverse problems, the multi-parameter Hessian is a very large matrix. Explicitly constructing multi-parameter Hessian is considered to be impractical. In this research, we propose to quantify the parameter resolution with multi-parameter point spread function, which is proportional to one column of the multi-parameter Hessian. With the multi-parameter point spread function, we quantity the parameter trade-offs among elastic parameters (P-wave velocity, S-wave velocity and density) more completely. These coupling effects are verified using numerical examples with reflection survey and transmission survey.

ELASTIC FULL-WAVEFORM INVERSION

In this section, we briefly review the theory of full-waveform inversion (FWI) methods. Full-waveform inversion (FWI) iteratively update the model parameters by minimizing a l-2 norm misfit function, which measures the differences between the modelled data $\mathbf{d}_{syn}\left(\mathbf{x}_s, \mathbf{x}_r, t; \mathbf{m}\right)$ and observed data $\mathbf{d}_{obs}\left(\mathbf{x}_s, \mathbf{x}_r, t\right)$. The misfit function can be expressed as:

$$\Phi\left(\mathbf{m}\right) = \sum_{s=1}^{S}\sum_{r=1}^{R}\int_0^T \|\Delta\mathbf{d}\left(\mathbf{x}_s, \mathbf{x}_r, t\right)\|^2 dt, \tag{1}$$

where $\Delta\mathbf{d}\left(\mathbf{x}_s, \mathbf{x}_r, t\right)$ is the data residual. With adjoint-state method, the gradient of the misfit function can be calculated by cross-correlating the forward modelling wavefield and backward propagated data residual wavefield. Considering the general elastic and anisotropic media, the gradients for density ρ and elastic coefficients c_{ijkl} can be expressed as:

$$\begin{aligned}\nabla_{\mathbf{m}}\Phi\left(\mathbf{m}\right) = -\sum_{s=1}^{S}\sum_{r=1}^{N}\int_0^T \left[d_i^{obs}\left(\mathbf{x}_s, \mathbf{x}_r, t\right) - d_i^{syn}\left(\mathbf{x}_s, \mathbf{x}_r, t\right)\right]\int_0^t\int_{\Omega(\mathbf{x})}\left[\delta\rho\left(\mathbf{x}\right)G_{ni}\left(\mathbf{x}, \mathbf{x}_r, T-t'\right)\partial_{t'}^2 u_i\left(\mathbf{x}_s, \mathbf{x}, t'\right)\right.\\ \left. + \Delta c_{ijkl}\left(\mathbf{x}\right)\partial_j' G_{ni}\left(\mathbf{x}, \mathbf{x}_r, t-t'\right)\partial_k' u_l\left(\mathbf{x}_s, \mathbf{x}, t'\right)\right]d^3\mathbf{x}dt'dt.\end{aligned} \tag{2}$$

The Fréchet derivative of the misfit function can be re-written as:

$$\nabla_{\mathbf{m}}\Phi\left(\mathbf{m}\right) = \int_{\Omega(\mathbf{x})}\left[K_\rho\left(\mathbf{x}\right)\Delta\rho\left(\mathbf{x}\right) + K_{c_{ijkl}}\Delta c_{ijkl}\left(\mathbf{x}\right)\right]d^3\mathbf{x}, \tag{3}$$

The 3-D waveform misfit kernels K_ρ and $K_{c_{jklm}}$ represent Fréchet derivatives with respect to density and the elastic parameters are defined by

$$K_\rho(\mathbf{x}) = -\sum_{s=1}^{S}\sum_{r=1}^{R}\int_0^T \Delta\rho(\mathbf{x})\,\mathbf{u}^\dagger(\mathbf{x}_r,\mathbf{x},T-t)\cdot\partial_t^2\mathbf{u}(\mathbf{x}_s,\mathbf{x},t)\,dt, \tag{4}$$

$$K_{c_{jklm}}(\mathbf{x}) = -\sum_{s=1}^{S}\sum_{r=1}^{R}\int_0^T\int \partial_j G_{ni}(\mathbf{x}_r,\mathbf{x},t-t')\,\Delta c_{ijkl}(\mathbf{x})\,\partial_k u_l(\mathbf{x},\mathbf{x}_s,t)\,dt'dt, \tag{5}$$

For an isotropic and elastic media, three parameters are needed to be inverted. The gradients for bulk modulus κ, shear modulus μ and density ρ are expressed as (Tromp et al., 2005; Yanhua et al., 2015):

$$\begin{aligned}
K_\kappa(\mathbf{x}) &= -\sum_{s=1}^{S}\sum_{r=1}^{R}\int_0^T \Delta\kappa(\mathbf{x})\,[\nabla\cdot\mathbf{u}^\dagger(\mathbf{x}_r,\mathbf{x},T-t)][\nabla\cdot\mathbf{u}(\mathbf{x}_s,\mathbf{x},t)]dt,\\
K_\mu(\mathbf{x}) &= -\sum_{s=1}^{S}\sum_{r=1}^{R}\int_0^T 2\Delta\mu(\mathbf{x})\,\mathbf{D}^\dagger(\mathbf{x}_r,\mathbf{x},T-t):\mathbf{D}(\mathbf{x}_s,\mathbf{x},t)\,dt,\\
K_\rho(\mathbf{x}) &= -\sum_{s=1}^{S}\sum_{r=1}^{R}\int_0^T \Delta\rho(\mathbf{x})\,\mathbf{u}^\dagger(\mathbf{x}_r,\mathbf{x},T-t)\cdot\partial_t^2\mathbf{u}(\mathbf{x}_s,\mathbf{x},t)\,dt,
\end{aligned} \tag{6}$$

where † represents adjoint simulation and $\mathbf{D}$ is the traceless strain deviator. In this research, we used the velocity parameterization for inversion. The sensitivity kernels of P-wave velocity α, S-wave velocity β and density ρ' are obtained as:

$$\begin{aligned}
K_\alpha(\mathbf{x}) &= 2\left(1+\frac{4\mu}{3\kappa}\right)K_\kappa(\mathbf{x}),\\
K_\beta(\mathbf{x}) &= 2\left(K_\mu(\mathbf{x})-\frac{4\mu}{3\kappa}K_\kappa(\mathbf{x})\right),\\
K_{\rho'}(\mathbf{x}) &= K_\rho(\mathbf{x})+K_\mu(\mathbf{x})+K_\kappa(\mathbf{x}).
\end{aligned} \tag{7}$$

Hessian operator, the second-order derivative of the misfit function, plays crucial role in full-waveform inversion. Applying the inverse Hessian to precondition the gradient can compensate the geometrical spreading and de-blur the gradient (Pratt et al., 1998; **?**; Pan et al., 2014, 2016c,a; Pan and Innanen, 2016). It has been proved that the off-diagonal blocks in multi-parameter Hessian can suppress the parameter crosstalk artifacts in gradients (Innanen, 2014; Pan et al., 2015, 2016b, 2017). Furthermore, the Hessian is also very important for uncertainty quantification in the inverse problems. In this research, we will show that the multi-parameter Hessian also carries essential information for understanding the parameter trade-off for multi-parameter FWI.

Joint elastic wave equation travel time and waveform inversion

Full-waveform inversion suffers from cycle-skipping difficulty results from the the lack of low frequencies and poor starting models. The non-linearity of the inverse problem

becomes much more serious when multiple physical parameters are needed to be recovered. In this report, we will practice the elastic wave equation trave time inversion method, which more linearly relates the model to the data. The cross-correlation misfit functions and adjoint sources can be found in Luo and Schuster (1991) and Zhou et al. (1997).

Parameter resolution issue

The parameter resolution issue has been studied by many researchers for multi-parameter FWI since Tarantola (1986), which help to select optimal parameterization and appropriate acquisition geometry for efficient multi-parameter FWI. However, these studies are based the analytic solutions of the Fréchet derivative wavefields due to different physical parameters. We find that these analyses may not be able to quantify the resolving abilities of different parameters completely. For obtaining the scattering patterns for different parameters, first, the background model is assumed to be isotropic and homogeneous and incident plane-wave with far-file approximation is assumed to be scattered due to local point heterogeneities or (horizonal reflector). In this condition, the geometrical spreading, finite-frequency effects and complex background are ignored. Hence, it is necessary to develop new techniques for parameter resolution analysis. In this paper, we revisit the parameter resolution issue for elastic FWI by probing the multi-parameter Hessian. The adjoint-state technique is employed to construct the column of the multi-parameter Hessian. With the multi-parameter point spread function, we are able to evaluate the spatial resolution and parameter trade-off by taking geometrical spreading, finite-frequency and complex model into consideration. To accelerate the iterative inversion algorithms, it is important to select parameters whose a posteriori uncertainties will be as uncorrelated as possible. A good choice of parameterization should give three diffractions which are as different as possible, to allow easy identification of the parameters.

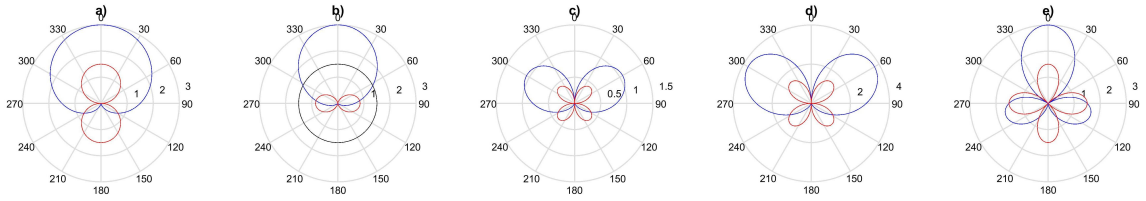

FIG. 1. (a), (b), (c), (d), and (e) show the SH-SH, P-P, P-SV, SV-P, SV-SV scattering patterns. The black, red and blue lines represent the scattering patterns due to P-wave velocity, S-wave velocity and density respectively.

NUMERICAL EXPERIMENTS

In this section, we carry our several numerical examples for understanding full-waveform inversion in elastic media. We first study the effects of density in elastic FWI and then illustrate numerical examples to show the effectiveness of wave equation travel time inversion for overcoming the cycle-skipping difficulty. We finally study the parameter resolution issue in elastic FWI via probing the multi-parameter Hessian.

Density effects

In this example, we apply full-waveform inversion to invert elastic parameters and study the role of density in elastic FWI with Marmousi model. Figures 2a-2c show the true P-wave velocity, S-wave velocity and density models. Figures 2d-2f show the corresponding initial P-wave velocity, S-wave velocity and density models. We first carry out elastic FWI by updating P-wave velocity, S-wave velocity and density simultaneously. Figures 3a-3c show the inverted P-wave velocity, S-wave velocity and density models. Figure 4 shows the convergence rate. As we can see, P-wave velocity and S-wave velocity can be reconstructed very well. However, density is poorly estimated.

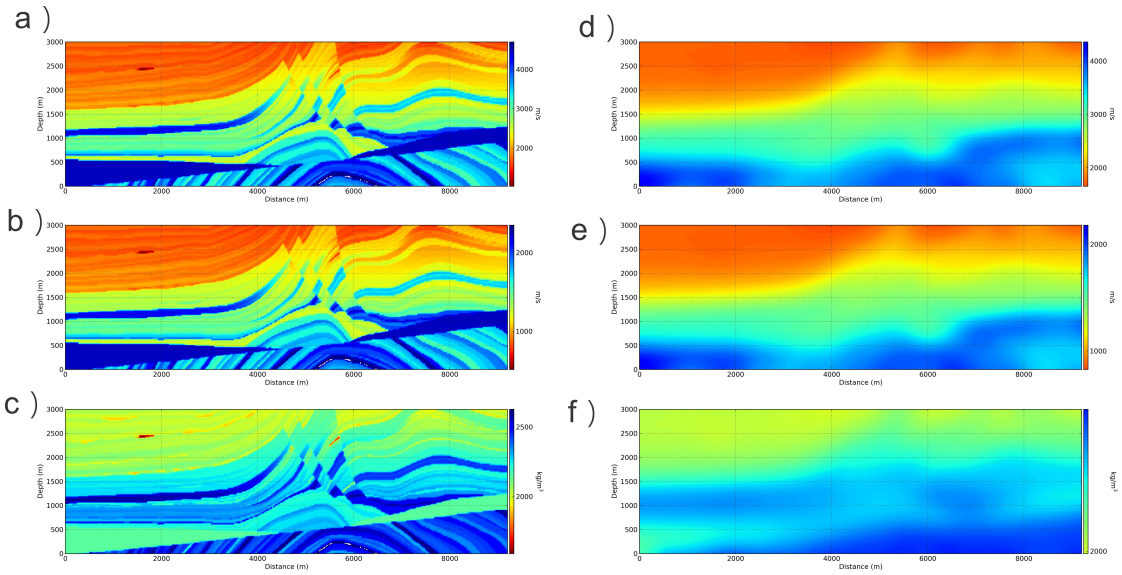

FIG. 2. (a), (b), and (c) show the true P-wave velocity, S-wave velocity, and density models. (d), (e), and (f) show the initial P-wave velocity, S-wave velocity, and density models.

We next carry out elastic FWI by updating P-wave velocity and S-wave velocity but keeping density unchanged. Figures 5a and 5b show the inverted P-wave velocity and S-wave velocity models. We observe that ignoring density, the P-wave velocity and S-wave velocity models can both be inverted very well. The inverted models are little better than those when updating P-wave velocity, S-wave velocity and density simultaneously. We then invert velocities and density models simultaneously using the inverted P-wave velocity and S-wave velocity models as initial models. Figure 7 shows the convergency history. The density model can be reconstructed better than previous one.

Joint elastic wave equation travel time and waveform inversion

In this example, we employ elastic wave equation travel time inversion for overcoming the cycle-skipping difficulty. We first give a simple example. Figures 8a and 8b show the true P-wave velocity and S-wave velocity models. The true velocity models consist of long wavenumber components with velocities increasing low to high linearly. The embedded Gaussian anomalies represent short wavenumber components of the velocity models. The initial P-wave velocity and S-wave velocity models are homogeneous.

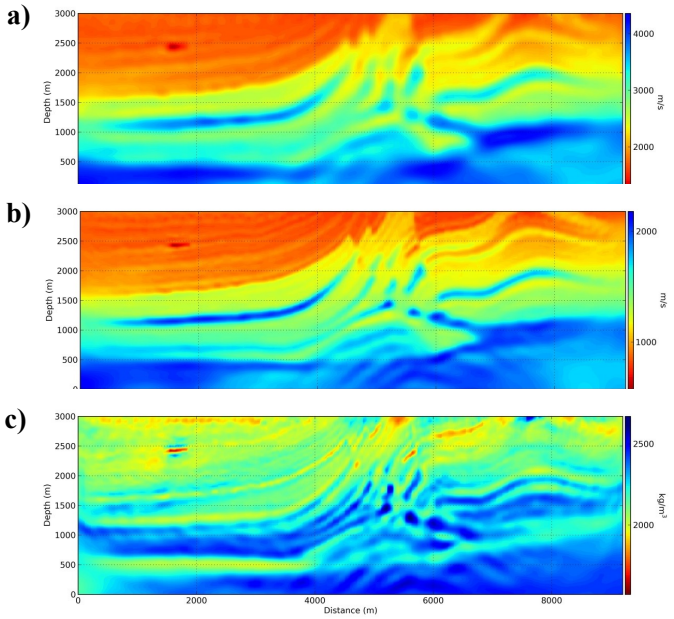

FIG. 3. (a), (b), and (c) show the inverted P-wave velocity, S-wave velocity, and density models.

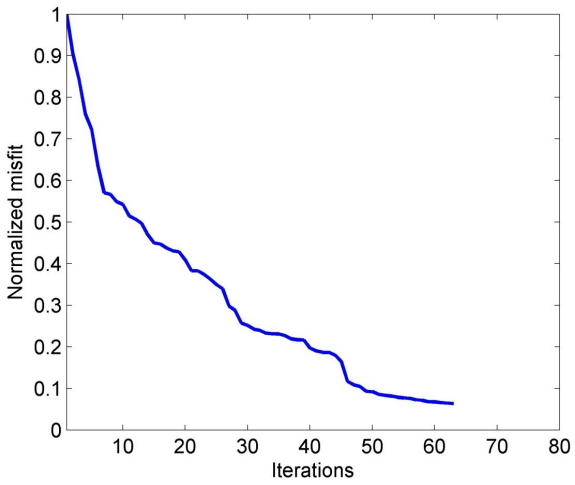

FIG. 4. Convergency rate.

We first try to invert P-wave and S-wave models using waveform inversion directly to show the problem of cycle-skipping in FWI. Figures 9a and 9b show the inverted P-wave velocity and S-wave velocity models. As we can see, the long wavenumber components of the models are not be retrieved and only the Gaussian anomalies are resolved. We next carry out the joint elastic wave equation travel time and waveform inversion method. The elastic wave equation travel time method is first used for inversion. As shown in Figures 10a and 10b, the long wavenumber components of the models have been recovered. We then use Figures 10a and 10b as initial models to invert P-wave velocity and S-wave velocity

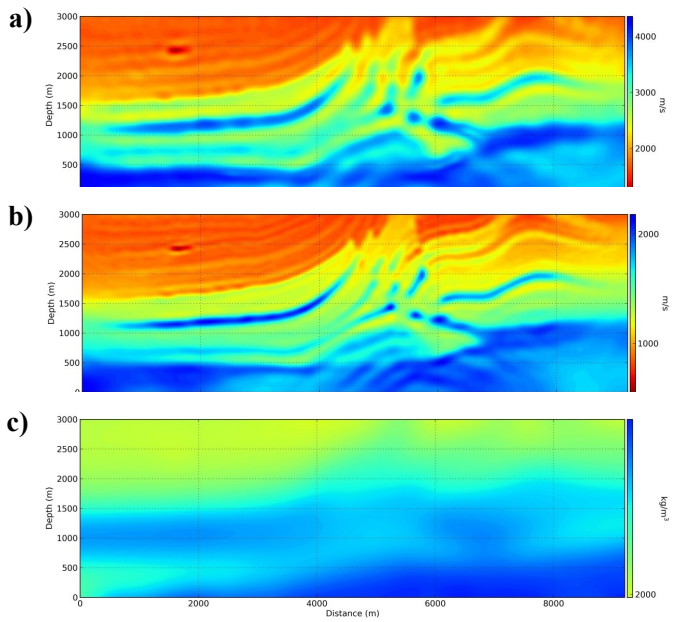

FIG. 5. (a), (b), and (c) show the inverted P-wave velocity, S-wave velocity, and density models.

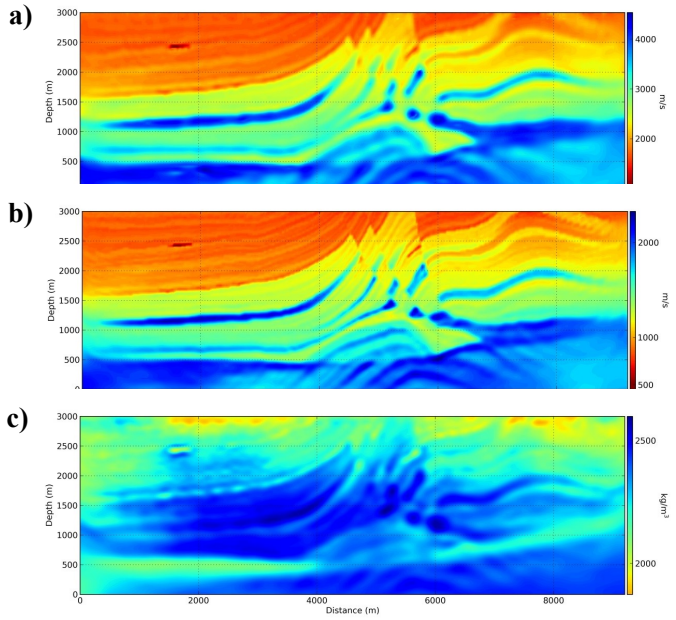

FIG. 6. (a), (b), and (c) show the inverted P-wave velocity, S-wave velocity, and density models.

using waveform inversion method. The inversion results are shown in Figures 11a and 11b. The cycle-skipping problem has been reduced and P-wave and S-wave velocity are inverted very well.

We then use a more complex Marmousi model to show the effectiveness of our method. The true model parameters are shown in Figure 2. In this example, we use poor models as initial guesses for elastic FWI, as shown in Figure 12. In the inversion process, we ignore the effects of density. Only P-wave velocity and S-wave velocity are updated and

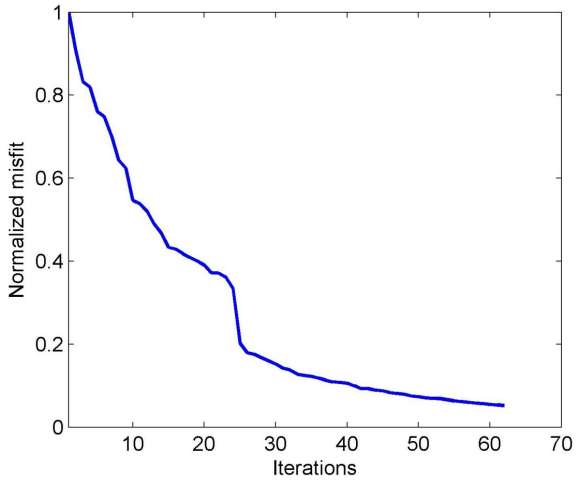

FIG. 7. Convergency history.

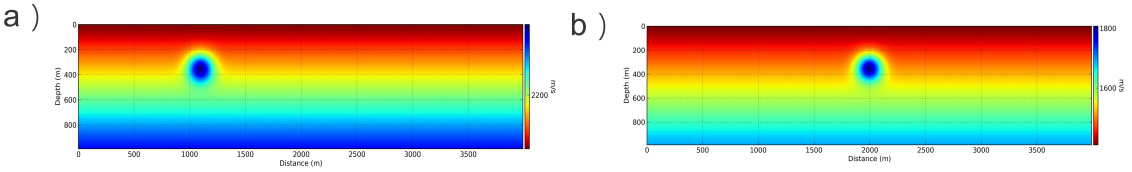

FIG. 8. (a) and (b) show the true P-wave velocity and S-wave velocity models respectively.

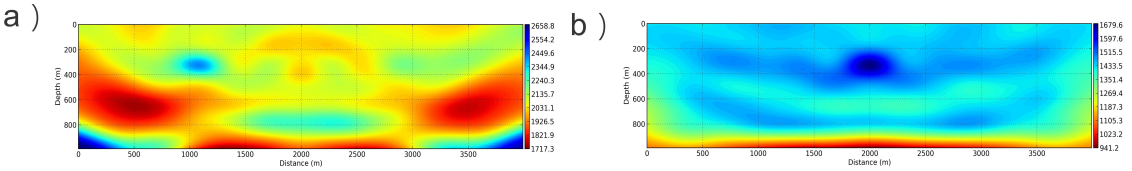

FIG. 9. (a) and (b) show the inverted P-wave velocity and S-wave velocity models using waveform inversion directly.

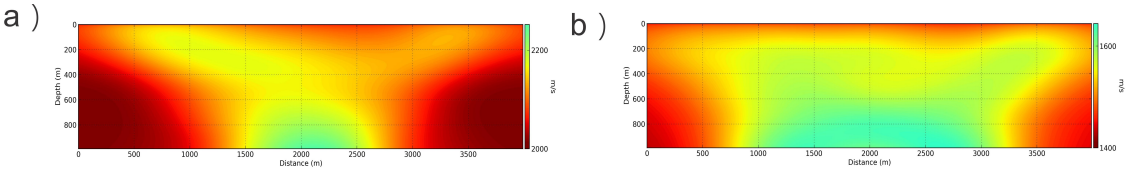

FIG. 10. (a) and (b) show the inverted P-wave velocity and S-wave velocity models using wave equation travel time inversion method.

density is kept as unchanged. Similarly, the waveform inversion method is employed for inversion first. As shown in Figures 13a and 13b, the inverted models are distorted and biased resulting from the lack of low frequencies and poor initial models. Figures 14a and 14b show the inverted P-wave and S-wave models using wave equation travel time inversion method. P-wave velocity model is better than S-wave velocity model. We observe that the shallow parts of the models have been constructed. Then, the inverted models are used as

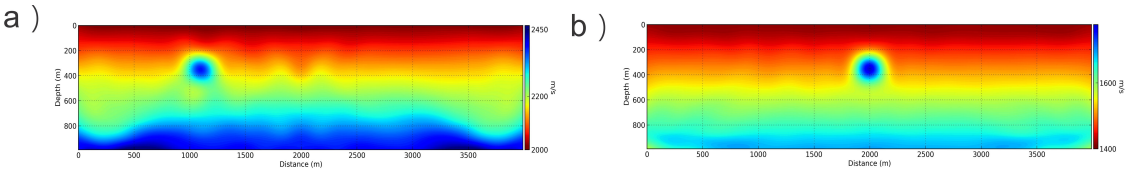

FIG. 11. (a) and (b) show the inverted P-wave velocity and S-wave velocity models obtained by waveform inversion using Figures 10a and 10b as initial models.

initial guesses in elastic waveform inversion. The inverted models are shown in Figures 15a and 15b. It can be seen that P-wave velocity and S-wave velocity models have been reconstructed much better. S-wave velocity is more resolved than P-wave velocity.

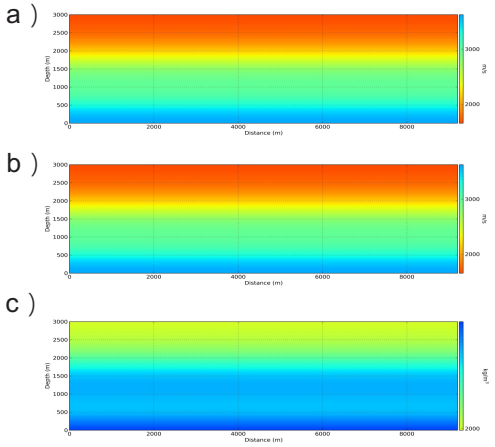

FIG. 12. (a) and (b) show the initial P-wave velocity and S-wave velocity models.

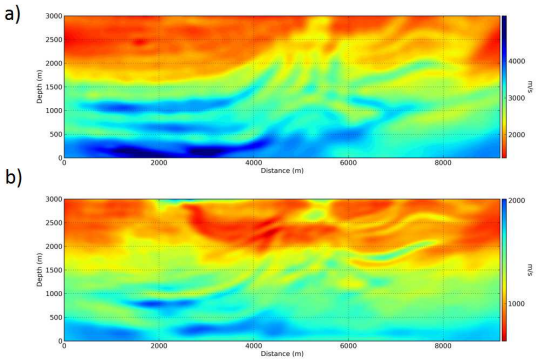

FIG. 13. (a) and (b) show the inverted P-wave velocity and S-wave velocity models using waveform inversion method directly.

Parameter resolution analysis by probing the multi-parameter Hessian

The coupling effects between different elastic parameters make the inverse problem much more non-linear. The parameter resolution studies based scattering patterns are not able to quantify the resolving abilities of different parameter classes completely. When taking S-wave into consideration, it is more complex and difficult to understand and interpret

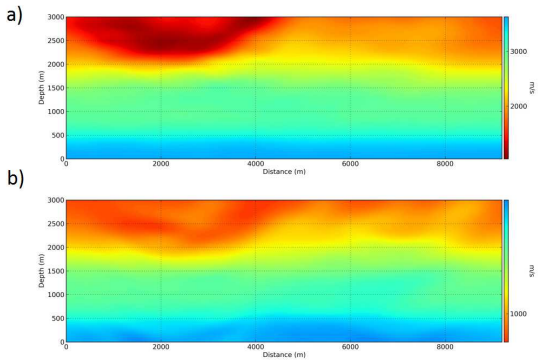

FIG. 14. (a) and (b) show the inverted P-wave velocity and S-wave velocity models using waveform inversion method directly.

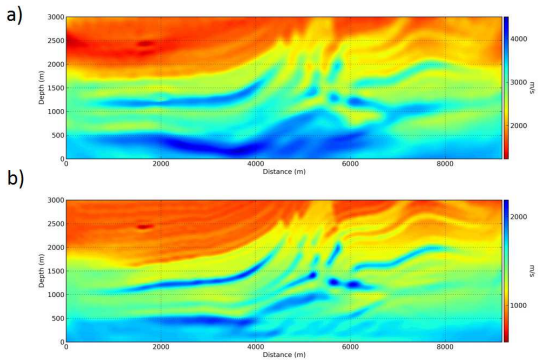

FIG. 15. (a) and (b) show the inverted P-wave velocity and S-wave velocity models using waveform inversion method directly.

the parameter trade-off. In this section, we studied the parameter resolution in elastic FWI by probing the multi-parameter Hessian, which provides direct measures of the parameter trade-offs. Note that the results presented in this section maybe different when using different measurements, different models, and different acquisition geometries.

We first calculate the multi-parameter point spread functions with a reflection survey. The model is homogeneous with P-wave velocity, S-wave velocity and density . A total of 64 sources are arranged from 65 m to 2855 m with a regular interval of 45 m and a depth of 15 m. A number of 295 receivers are deployed from 30 m to 2970 m with a depth of 15 m. We first apply a point perturbation of P-wave velocity at (1500m, 500m) and keep other parameter unchanged. The gradients for P-wave velocity, S-wave velocity and density are calculated as shown in Figures 16a-16c. The gradients due to the point perturbation of P-wave velocity are proportional to one column of the multi-parameter Hessian. Figures 16b and 16c represent the mapping from P-wave to S-wave velocity and density. We then calculate the gradients due point perturbations of S-wave velocity and density, as illustrated from Figure 16d to Figure 16i. Figure 16 show three columns in multi-parameter Hessian corresponding to P-wave velocity, S-wave velocity and density. Figures 16d and 16f represent the mapping from S-wave velocity to P-wave velocity and density. Figures 16g and 16h represent the mapping from density to P-wave velocity and S-wave velocity.

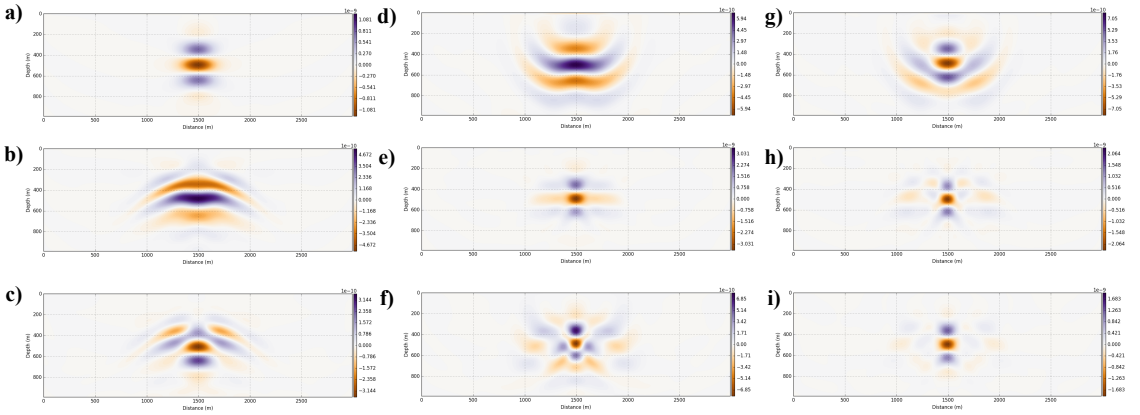

FIG. 16. (a), (b) and (c) show the multi-parameter point spread functions due to the point perturbation of P-wave velocity; (d), (e) and (f) show the multi-parameter point spread functions due to the point perturbation of S-wave velocity; (g), (h) and (i) show the multi-parameter point spread functions due to the point perturbation of density.

Figure 17 show the multi-parameter point spread functions after normalization. In this condition, we are able to evaluate the inter-parameter mapping among these parameters. As we can see, the mapping from P-wave velocity to S-wave velocity and density are pretty weak. However, the mappings from S-wave velocity to density and P-wave velocity are strong. The mappings from density to P-wave velocity and density are also strong. To verify our predictions, we carry out numerical experiments. The true P-wave velocity, S-wave velocity and density models are shown in Figures 18a, 18b, and 18c respectively. The Gaussian anomalies in the true models are uncorrelated. The initial models are homogeneous. Figures 19a, 19b and 19c show the gradients for P-wave velocity, S-wave velocity and density respectively. The mappings from S-wave velocity and density perturbations to P-wave velocity gradient are strong. We also observe that there are strong mappings from density to S-wave velocity and P-wave velocity. For the reflection survey, we see that the mapping from S-wave velocity to P-wave velocity is quickly suppressed with updating S-wave velocity. In previous Marmousi example, we notice that density is quite difficult to be reconstructed. However, in this example, the density is recovered very well. This maybe caused by that density is sensitive to amplitude but not sensitive to travel time. In this Gaussian anomalies example, the travel time perturbations due to model perturbations are not large. These observations verify our predictions using multi-parameter Hessian.

We next present an example with a transmission survey. The receivers are moved to the depth of 985 m. The true and initial models are the same with previous example. Similarly, we calculate the multi-parameter point spread functions with this transmission survey, as shown in Figure 22 and Figure 23 (after normalization). From Figure 23, we predict that the mapping from P-wave velocity to S-wave velocity will be weak. While the mapping from P-wave velocity to density will be a little stronger. The mapping from S-wave velocity to P-wave velocity is not so strong. However, the mapping from S-wave velocity to density will be very strong. The mappings from density to P-wave velocity and S-wave velocity will be very weak and can be ignored.

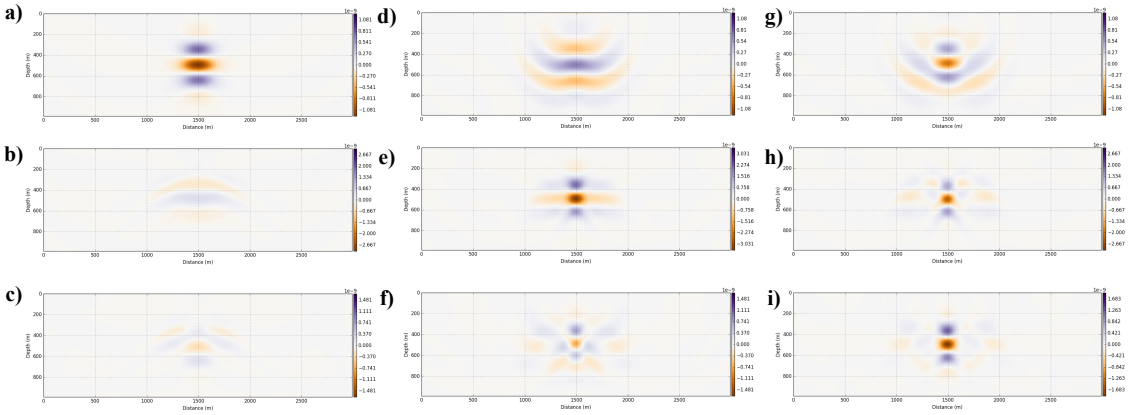

FIG. 17. Multi-parameter point spread functions after normalization.

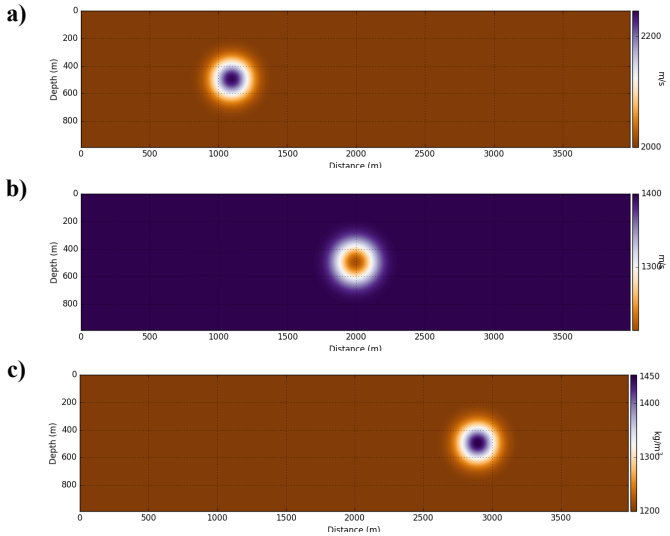

FIG. 18. (a), (b) and (c) show the true P-wave velocity, S-wave velocity and density models.

We then carry out the inversion with this transmission survey. Figures 24a, 24b, and 24c show the gradient updates for the P-wave velocity, S-wave velocity and density models. In the gradient update for P-wave velocity, we see that the parameter crosstalk artifacts due to S-wave and density are weak. In the gradient update for S-wave velocity, we can not observe the parameter crosstalk artifacts due to P-wave velocity and density. In the inverted density mode, the parameter crosstalk artifacts from S-wave velocity are very strong, which makes that the true update for density can be ignored. P-wave velocity perturbation also produces artifacts in the density update. Figures 25a, 25b, and 25c show the inverted P-wave velocity, S-wave velocity and density models after 2 iterations. Figures 26a, 26b, and 26c show the inverted P-wave velocity, S-wave velocity and density models after 7 iterations. The P-wave velocity and S-wave velocity models are recovered very well and the parameter crosstalk artifacts can be ignored. However, the inverted density model is contaminated by parameter crosstalk artifacts seriously, especially due to S-wave velocity.

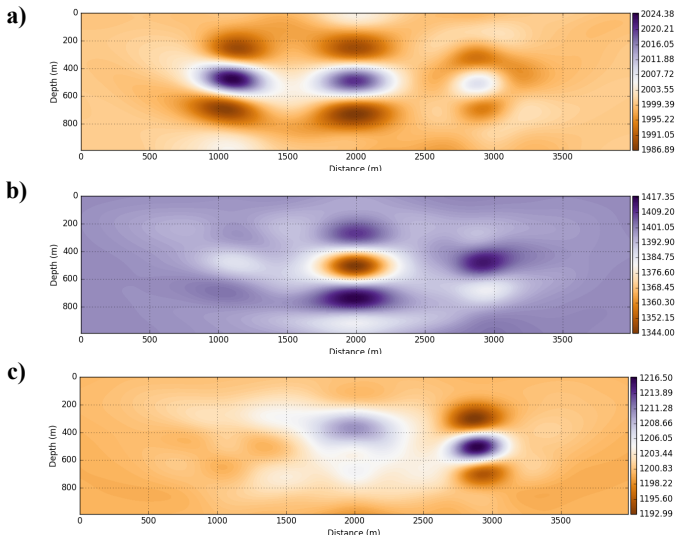

FIG. 19. (a), (b) and (c) show the gradient updates for P-wave velocity, S-wave velocity and density.

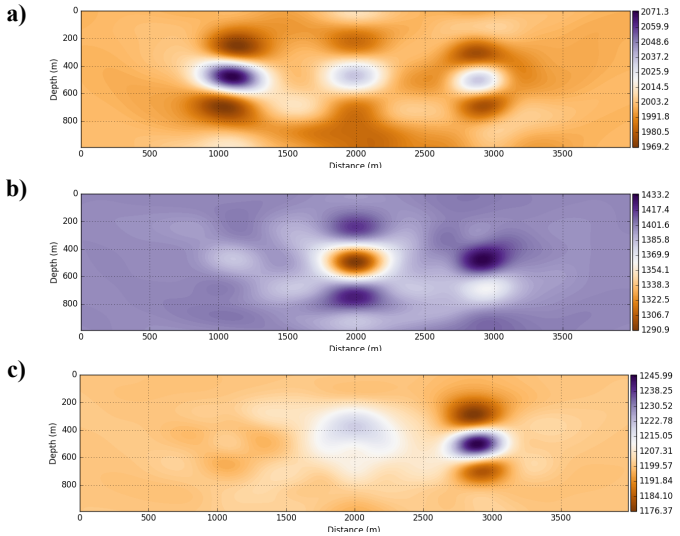

FIG. 20. (a), (b) and (c) show the inverted P-wave velocity, S-wave velocity and density models after 2 iterations.

These inversion results verify our predications by probing of the multi-parameter Hessian.

CONCLUSION

In this research, we practice elastic FWI for examining the density effects and joint elastic wave equation travel time and waveform inversion method. We find that the density does not . With the elastic wave equation travel time inversion methods, the long wavenumber components of the velocity models can be reconstructed, which help to overcome the cycle-skipping difficulty in elastic FWI. We also propose to quantify the parameter resolution for multi-parameter FWI using multi-parameter Hessian. The numerical examples are given the verify our ideas.

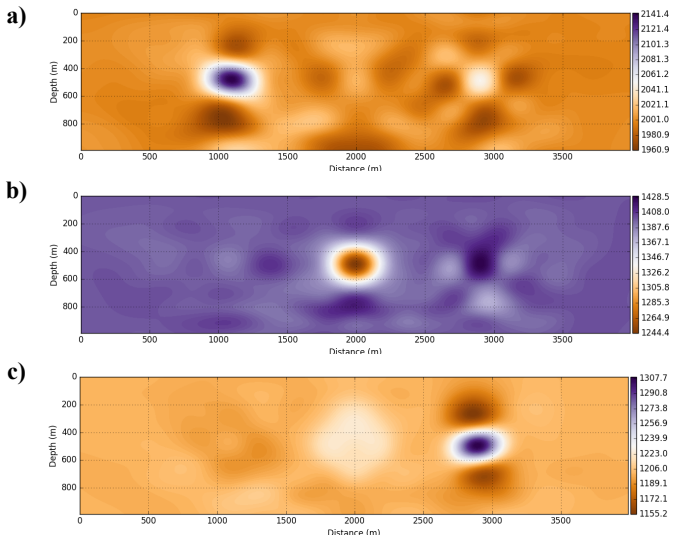

FIG. 21. (a), (b) and (c) show the inverted P-wave velocity, S-wave velocity and density models after 5 iterations.

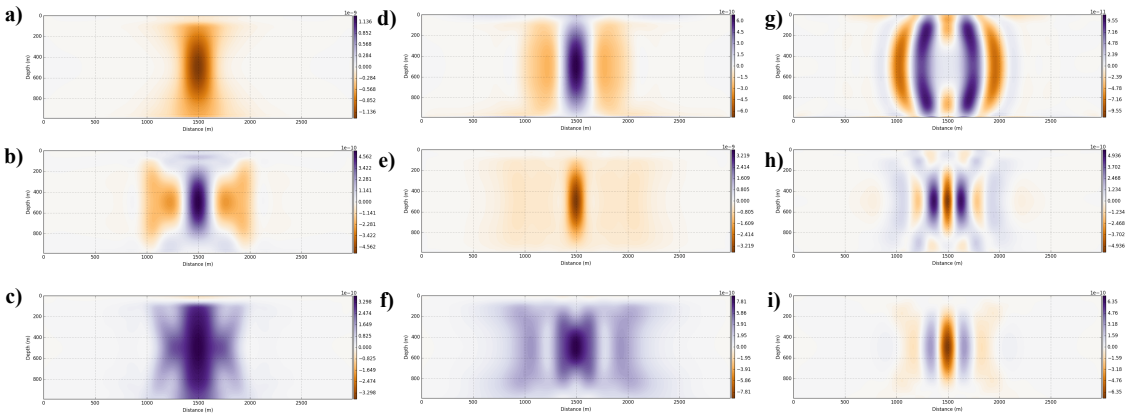

FIG. 22. Multi-parameter point spread functions after normalization.

ACKNOWLEDGEMENTS

The authors thank the sponsors of CREWES for continued support. This work was funded by CREWES industrial sponsors and NSERC (Natural Science and Engineering Research Council of Canada) through the grant CRDPJ 461179-13. Author 1 was also supported by a SEG/Chevron scholarship. We greatly thanks to Yanhua Yan of Princeton University for helping me practice elastic FWI using specfem2d and seisDD. Thanks sincerely to Prof. Frederik Simons for his insightful comments and suggestions. Thanks also to Jeroen Tromp for allowing me to use the high-performance computing facilities at Princeton University. Thanks also toYouyi Ruan, Wenjie Lei, Ryan Modark, Dmitry Borisov and James Smith for their helpful discussions.

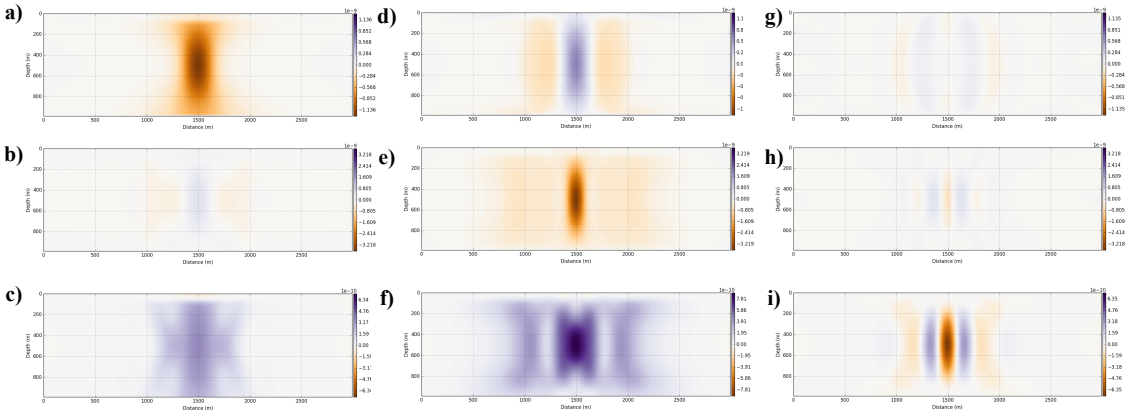

FIG. 23. Multi-parameter point spread functions after normalization.

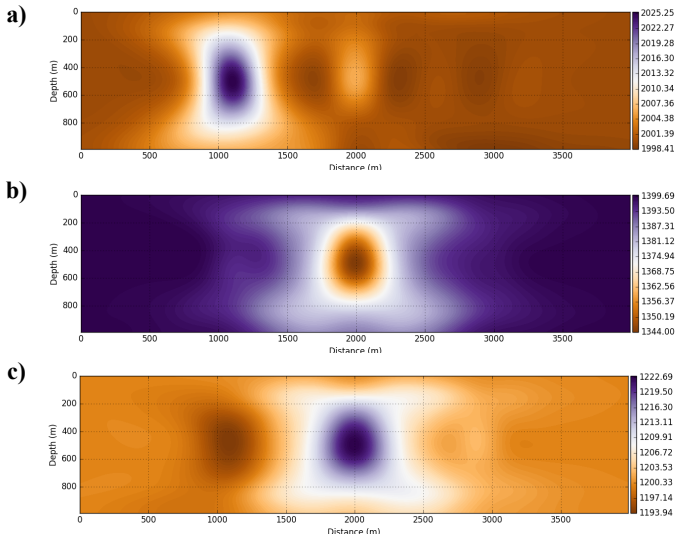

FIG. 24. (a), (b) and (c) show the gradient updates for P-wave velocity, S-wave velocity and density.

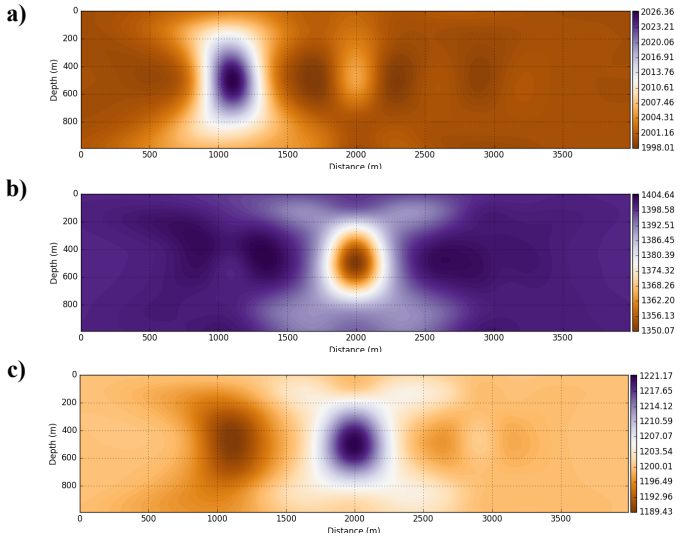

FIG. 25. (a), (b) and (c) show the inverted P-wave velocity, S-wave velocity and density after 2 iterations.

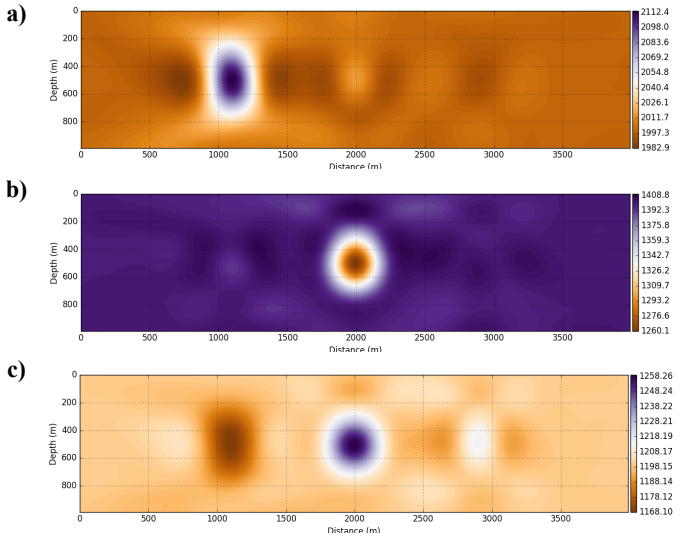

FIG. 26. (a), (b) and (c) show the inverted P-wave velocity, S-wave velocity and density after 7 iterations.

REFERENCES

Innanen, K. A., 2014, Seismic AVO and the inverse Hessian in precritical reflection full waveform inversion: Geophysical Journal International, **199**, 717–734.

Lailly, P., 1983, The seismic inverse problem as a sequence of before stack migration: Conference on Inverse Scattering, Theory and Applications, SIAM, Expanded Abstracts, 206–220.

Li, Y., and Demanet, L., 2016, Full-waveform inversion with extrapolated low-frequency data: Geophysics, **81**, R339–R348.

Luo, Y., and Schuster, G. T., 1991, Wave-equation traveltime inversion: Geophysics, **56**, 645–653.

Ma, Y., and Hale, D., 2012, Quasi-Newton full-waveform inversion with a projected Hessian matrix: Geophysics, **77**, R207–R216.

Pan, W., and Innanen, K. A., 2016, A summary of several challenges facing multi-parameter elastic full waveform inversion: CSEG Recorder, 36–39.

Pan, W., Innanen, K. A., and Liao, W., 2016a, Accelerating Hessian-free Gauss-Newton full-waveform inversion via improved preconditioning strategies: SEG Expanded Abstracts, 1455–1461.

Pan, W., Innanen, K. A., and Liao, W., 2017, Accelerating Hessian-free Gauss-Newton full-waveform inversion via l-BFGS preconditioned conjugate-gradient algorithm: Geophysics, 1–10.

Pan, W., Innanen, K. A., and Margrave, G. F., 2014, A comparison of different scaling methods for least-squares migration/inversion: EAGE Expanded Abstracts, We G103 14.

Pan, W., Innanen, K. A., Margrave, G. F., Fhler, M. C., Fang, X., and Li, J., 2015, Estimation of elastic constants in HTI media using Gauss-Newton and Full-Newton multi-parameter full waveform inversion: SEG Technical Program Expanded Abstracts, 1177–1182.

Pan, W., Innanen, K. A., Margrave, G. F., Fhler, M. C., Fang, X., and Li, J., 2016b, Estimation of elastic constants for HTI media using Gauss-Newton and full-Newton multiparameter full-waveform inversion: Geophysics, **81**, R275–R291.

Pan, W., Innanen, K. A., Margrave, G. F., and Keating, S., 2016c, Mitigate cycle-skipping for full-waveform inversion by band-limited impedance inversion and POCS: GeoConvention, 1–5.

Pratt, R. G., Shin, C., and Hicks, G. J., 1998, Gauss-Newton and full Newton methods in frequency-space seismic waveform inversion: Geophysical Journal International, **133**, 341–362.

Tarantola, A., 1984, Inversion of seismic reflection data in the acoustic approximation: Geophysics, **49**, 1259–1266.

Tarantola, A., 1986, A strategy for nonlinear elastic inversion of seismic reflection data: Geophysics, **51**, 1893–1903.

Tromp, J., Tape, C., and Liu, Q., 2005, Seismic tomography, adjoint methods, time reversal, and banana-doughnut kernels: Geophysical Journal International, **160**, 195–216.

Virieux, A., and Operto, S., 2009, An overview of full-waveform inversion in exploration geophysics: Geophysics, **74**, WCC1–WCC26.

Warner, M., and Guasch, L., 2014, Adaptive waveform inversion: theory: SEG Expanded Abstracts, 1089–1093.

Wu, W., Luo, J., and Wu, B., 2014, Seismic envelope inversion and modulation signal model: Geophysics, **79**, WA13–WA24.

Yanhua, Y. O., and Simons, F. J., 2014, Multiscale adjoint waveform-difference tomography using wavelets: Geophysics, **79**, WA79–WA95.

Yanhua, Y. O., Simons, F. J., and Bozdağ, E., 2015, Multiscale adjoint waveform tomography for surface and body waves: Geophysics, **80**, R281–R302.

Zhou, C., Schuster, G. T., Hassanzadeh, S., and Harris, J. M., 1997, Elastic wave equation traveltime and waveform inversion of crosswell data: Geophysics, **62**, 853–868.

Zhu, H., and Fomel, S., 2016, Building good starting models for full-waveform inversion using adaptive matching filtering misfit: Geophysics, **81**, U61–U72.